EPR and X-ray Crystallographic Characterization of the Product-Bound Form of the Mn^{II}-Loaded Methionyl Aminopeptidase from *Pyrococcus furiosus*[†,‡]

Alicja J. Copik,[§] Boguslaw P. Nocek,[||] Sabina I. Swierczek,[§] Shane Ruebush,[§] Se Bok Jang,[||] Lu Meng,[§] Ventris M. D'souza,[§] John W. Peters,[||] Brian Bennett,[⊥] and Richard C. Holz*[,§]

Department of Chemistry and Biochemistry, Utah State University, Logan, Utah 84322-0300, the Department of Chemistry and Biochemistry, Montana State University, Bozeman, Montana 59717, and Department of Biophysics, The Medical College of Wisconsin, Milwaukee, Wisconsin 53226-0509

Received August 31, 2004; Revised Manuscript Received October 22, 2004

ABSTRACT: Methionine aminopeptidases (MetAPs) are ubiquitous metallohydrolases that remove the N-terminal methionine from nascent polypeptide chains. Although various crystal structures of MetAP in the presence of inhibitors have been solved, the structural aspects of the product-bound step has received little attention. Both perpendicular- and parallel-mode electron paramagnetic resonance (EPR) spectra were recorded for the Mn^{II}-loaded forms of the type-I (*Escherichia coli*) and type-II (*Pyrococcus furiosus*) MetAPs in the presence of the reaction product L-methionine (L-Met). In general, similar EPR features were observed for both [MnMn(*Ec*MetAP-I)]−L-Met and [MnMn(*Pf*MetAP-II)]−L-Met. The observed perpendicular-mode EPR spectra consisted of a six-line hyperfine pattern at $g = 2.03$ ($A = 8.8$ mT) with less intense signals with eleven-line splitting at $g = 2.4$ and 1.7 ($A = 4.4$ mT). The former feature results from mononuclear, magnetically isolated Mn^{II} ions and this signal are 3-fold more intense in the [MnMn(*Pf*MetAP-II)]−L-Met EPR spectrum than in the [MnMn(*Ec*MetAP-I)]−L-Met spectrum. Inspection of the EPR spectra of both [MnMn(*Ec*MetAP-I)]−L-Met and [MnMn(*Pf*MetAP-II)]−L-Met at 40 K in the parallel mode reveals that the [Mn(*Ec*MetAP-I)]−L-Met spectrum exhibits a well-resolved hyperfine split pattern at $g = 7.6$ with a hyperfine splitting constant of $A = 4.4$ mT. These data suggest the presence of a magnetically coupled dinuclear Mn^{II} center. On the other hand, a similar feature was not observed for the [MnMn(*Pf*MetAP-II)]−L-Met complex. Therefore, the EPR data suggest that L-Met binds to [MnMn(*Ec*MetAP-I)] differently than [MnMn(*Pf*MetAP-II)]. To confirm these data, the X-ray crystal structure of [MnMn(*Pf*MetAP-II)]−L-Met was solved to 2.3 Å resolution. Both Mn1 and Mn2 reside in a distorted trigonal bipyramidal geometry, but the bridging water molecule, observed in the [CoCo(*Pf*MetAP-II)] structure, is absent. Therefore, L-Met binding displaces this water molecule, but the carboxylate oxygen atom of L-Met does not bridge between the two Mn^{II} ions. Instead, a single carboxylate oxygen atom of L-Met interacts with only Mn1, while the N-terminal amine nitrogen atom binds to M2. This L-Met binding mode is different from that observed for L-Met binding [CoCo(*Ec*MetAP-I)]. Therefore, the catalytic mechanisms of type-I MetAPs may differ somewhat from type-II enzymes when a dinuclear metalloactive site is present.

Methionine aminopeptidases (MetAPs) are ubiquitous enzymes that are responsible for the removal of N-terminal methionine residues from newly synthesized polypeptide chains (*1*−*5*). While the rationale for the removal of the initiator methionine remains unclear, several explanations have been proposed (*4*). Some involve the facilitation of further processing after excision of the N-terminal group such as removal of signal sequences if present, proteolytic cleavage to generate shorter peptides, and/or the covalent attachment of residues and blocking groups such as acetyl and myristoyl groups (*3*). MetAPs are, therefore, one of the key cellular enzymes involved in protein maturation. Deletion of the gene encoding for MetAPs has been shown to be lethal to *Escherichia coli*, *Saccharomyces cerevisiae*, and *Salmonella typhimurium*, indicating that the activity of MetAP is essential for cell growth and survival (*6*−*8*). The importance of understanding the catalytic mechanism of MetAPs is underscored by the recent observation that MetAPs are the target for antiangiogenesis drugs, one of which is in third stage clinical trials (*9*, *10*). Thus, the design of mechanism-based inhibitors is critically important in the development of drugs that prevent tumor vasculature formation, growth, and proliferation.

On the basis of sequence alignment and X-ray crystallography data, MetAPs have been divided into two classes (types I and II), distinguished by an extra 62 amino acid

[†] This work was supported in part by the National Institutes of Health (GM-56495 to R.C.H. and AI-056231 to B.B.), National Science Foundation (CHE-0240810 to R.C.H.), and Thermal Biology Institute at Montana State University (NAG5-8807 to J.W.P.). J.W.P. is a recent recipient of a Camille Dreyfus Teacher/Scholar Award.

[‡] The RCSB Protein Data Bank accession code for atomic coordinates is 1WKM.

* To whom correspondence should be addressed: Department of Chemistry and Biochemistry, Utah State University, Logan, UT 84322-0300. Telephone: (435) 797-2609. Fax: (435) 797-3390. E-mail: rholz@cc.usu.edu.

[§] Utah State University.

[||] Montana State University.

[⊥] The Medical College of Wisconsin.

10.1021/bi048123+ CCC: $30.25
Published on Web 12/13/2004

helical subdomain inserted within the C-terminal domain in type-II enzymes, of unknown function (*11*). Bacteria have only type-I MetAPs, while archaea contain only type II. In contrast, eukaryotes contain both type-I and type-II MetAPs (*1*). The type-I MetAPs from *E. coli* (*Ec*MetAP-I)[1] and *Staphylococcus aureus* (*Sa*MetAP-I) and the type-II MetAPs from *Pyrococcus furious* (*Pf*MetAP-II) and *Homo sapiens* (*Hs*MetAP-II) have been crystallographically characterized and shown to contain homologous catalytic domains that contain two metal ions coordinated by strictly conserved residues: two glutamates, two aspartates, a histidine, and two water molecules (*12*−*16*). Although crystallographic analyses together with sequence comparisons initially led to the supposition that all MetAPs were cobalt-dependent dinuclear hydrolases, recent work has questioned the validity of this assumption (*17*−*20*). It has been shown that *Ec*MetAP-I and *Pf*MetAP-II can be fully activated by a single equivalent of Co^{II}, even though both enzymes can incorporate 2 equiv of Co^{II} (*19*, *20*). However, the two metal-binding affinities differ by over 3 orders of magnitude, suggesting that MetAPs are mononuclear hydrolases *in vivo* (*19*). The higher affinity, catalytically relevant divalent metal-binding site has been assigned to the histidine-containing site based on ^{1}H NMR (*19*) and EXAFS (*21*) data.

MetAPs can be activated to different degrees by several first-row divalent transition-metal ions, which has raised the question regarding the identity of the physiologically relevant metal. Walker et al. suggested that Zn^{II} is the physiologically relevant metal for the yeast MetAP-I because the enzyme was maximally activated with zinc in the presence of 1 mM EDTA and glutathione (*17*). In contrast, *in vitro* activity assays and whole-cell metal analyses by D'souza et al. (*18*) suggested that Fe^{II} or Mn^{II} is the *in vivo* metal ion for *Ec*MetAP-I. Iron has also been shown to maximally activate *Pf*MetAP-II and provides a particularly active enzyme form at 80 °C, the physiologically relevant temperature for *P. furious* (*20*). This observation suggests a physiological role for Fe^{II} in *Pf*MetAP-II. In more recent studies, the *in vivo* inhibition of *Hs*MetAP-II by two competitive inhibitors, one of which is specific for Mn^{II}-loaded *Hs*MetAP-II, was characterized and these data suggested that Mn^{II} is the active-site metal *in vivo* (*22*).

Because recent studies have highlighted manganese as a plausible candidate for the *in vivo* divalent metal ion (*22*), it is important to provide insight into the mode of Mn^{II} binding to the active site of both type-I and type-II MetAPs. In an effort to gain structural and mechanistic information on the Mn^{II}-loaded forms of MetAPs, electron paramagnetic resonance (EPR) spectra of [MnMn(*Pf*MetAP-II)] and [MnMn(*Ec*MetAP-I)] were recorded in the absence and presence of the product of hydrolysis, L-methionine (L-Met). In addition, the X-ray crystal structure of the [MnMn(*Pf*MetAP-II)]−L-Met complex was solved to 2.3 Å resolution. Differences between the binding mode of L-Met to [MnMn(*Pf*MetAP-II)] versus both [MnMn(*Ec*MetAP-I)] and [CoCo(*Ec*MetAP-I)] and their mechanistic implications are discussed.

MATERIALS AND METHODS

Protein Expression and Purification. Recombinant *Ec*MetAP-I (Arg175Gln) was expressed and purified as previously described (*18*). Purified *Ec*MetAP-I exhibited a single band on SDS−PAGE and a single symmetrical peak in matrix-assisted laser desorption ionization−time-of-flight (MALDI−TOF) mass spectrometric analysis indicating $M_r = 29\,630 \pm 10$. Protein concentrations for all experiments were estimated from the absorbance at 280 nm using an extinction coefficient of 16 450 M^{-1} cm^{-1}. Apo-*Ec*MetAP-I samples were exchanged into 25 mM [4-(2-hydroxyethyl)-1-piperazineethanesulfonic acid] (HEPES) at pH 7.5, containing 150 mM KCl (Centricon-10, Millipore Corp.).

*Pf*MetAP-II was purified as previously reported (*20*). Purified *Pf*MetAP-II exhibited a single band on SDS−PAGE with a M_r of 33 000. Protein concentrations were estimated from the absorbance at 280 nm using an extinction coefficient of 21 650 M^{-1} cm^{-1}. Metal-free *Pf*MetAP-II was prepared by concentrating the as-purified *Pf*MetAP-II to a volume of ∼5 mL after which EDTA was added to a final concentration of 10 mM. The resulting protein solution was dialyzed against 25 mM HEPES (2 L, pH 7.5) containing 10 mM EDTA and 150 mM KCl at 4 °C for 2 days with two buffer changes per day. The protein solution was then dialyzed against chelexed (Chelex-100 Column) 25 mM HEPES buffer (2L, pH 7.5) containing 150 mM KCl for 3 days against two buffer changes per day. The resulting *Pf*MetAP-II was inactive and was found to contain no detectable metal ions via inductively coupled plasma−atomic emission spectrometry (ICP−AES).

Enzymatic Assay. *Ec*MetAP-I was assayed for catalytic activity with the tetrapeptide MGMM as the substrate (8 mM) using a high-performance liquid chromatography (HPLC) method as previously described (*19*). This method is based on the spectrophotometric quantitation of the reaction product GMM following separation on a C8 HPLC column (Phenomenex, Luna; 5 m, 4.6 × 25 cm). The kinetic parameter v (velocity) was determined at pH 7.5 by quantifying the tripeptide GMM at 215 nm in triplicate. The inhibition constant (K_i) for L-Met (from Sigma, St. Luis, MO) was obtained by measuring the activity of 1 μM of Mn^{II}-loaded *Pf*MetAP-II with 1−30 mM MGMM in the presence of 0−200 mM L-Met. These data were fit to the nonlinear competitive inhibition equation, using Sigma Plot Software.

Spectroscopic Measurements. Electronic absorption spectra were recorded on a Hewlett−Packard (8453) diode array spectrophotometer. Low-temperature EPR spectroscopy was performed using a Bruker ESP-300E spectrometer equipped with an ER 4116 DM dual mode X-band cavity and Oxford Instruments ESR-900 helium flow cryostat. Background spectra, recorded on a buffer sample, were aligned with and subtracted from all experimental spectra. EPR spectra were recorded at microwave frequencies of ∼9.65 GHz, and precise microwave frequencies were recorded for individual spectra to ensure precise g alignment. All spectra were recorded at 100 kHz modulation frequency, while other EPR

[1] Abbreviations: *Ec*MetAP-I, methionyl aminopeptidase from *E. coli*; *Pf*MetAP-II, methionyl aminopeptidase from *Pyrococcus furiosus*; *Hs*MetAP-II, methionyl aminopeptidase from *Homo sapiens*; MALDI−TOF, matrix-assisted laser desorption ionization−time of flight; HEPES, [4-(2-hydroxyethyl)-1-piperazineethanesulfonic acid]; ICP−AES, inductively coupled plasma−atomic emission spectroscopy; HPLC, high-performance liquid chromatography; AAP, aminopeptidase from *Aeromonas proteolytica*; MGMM, Met-Gly-Met-Met; EPR, electron paramagnetic resonance; L-Met, L-methionine; TFA, trifluoroacetic acid.

Table 1: Data and Refinement Statistics of the [MnMn(*Pf*MetAP-II)]−L-Met Structure[a]

crystals	*Pf*MetAP-II
space group	$P6_4$
cell dimensions	$a = 112.01$ Å
	$b = 112.01$ Å
	$c = 122.96$ Å
resolution (Å)	30.0−2.30
completeness (%) (last cell)	99.7 (99.9)
observed reflections	208 524
unique reflections	38 795
I/σ	4.4 (2.6)
R_{merge} (%)[b]	11.0 (33.5)
protein nonhydrogen atoms	4620
solvent molecules	325
Mn ions	4.0
R_{cryst} (%)[c]	21.5
R_{free} (%)[c]	25.2
bond lengths (Å)	0.011
bond angles (deg)	2.2
Ramachandran analysis	
most favored regions (%)	92.2
additional allowed regions	7.4
generously allowed regions	0.4
disallowed regions	0.0

[a] Numbers in parentheses indicate values for the highest resolution bin. [b] $R_{merge} = \sum_{hkl}\sum_i|I_i - \langle I\rangle|/\sum_{hkl}\sum_i|\langle I\rangle|$, where I_i is the intensity for the ith measurement of an equivalent reflection with indices h, k, and l. [c] $R_{cryst} = \sum_{hkl}||F_{obs}| - |F_{calc}||/\sum_{hkl}|F_{obs}|$, where F_{obs} denotes the observed structure-factor amplitude and F_{calc} denotes the structure-factor amplitude calculated from the model; 5% of the reflections were used to calculate [b]R_{free}.

Table 2: Selected Averaged Distances for the Active Site of [MnMn(*Pf*MetAP-II)]−L-Met and the Analogous Distances for [CoCo(*Ec*MetAP-I]−L-Met[a]

	A	*B*	average		
Mn(1)−Mn(2)	3.34	3.45	3.4	Co(1)−Co(2)	3.3
Mn(1)−Asp93(O_{δ^2})	1.94	2.04	2.0	Co(1)−Asp108(O_{δ^1})	2.0
Mn(1)−His153(N_{ϵ^2})	2.13	2.13	2.1	Co(1)−His171(N_{ϵ^2})	2.1
Mn(1)−Glu187(O_{ϵ^2})	2.12	2.04	2.1	Co(1)−Glu204(O_{ϵ^2})	2.1
Mn(1)−Glu280(O_{ϵ^2})	1.96	2.00	2.0	Co(1)−Glu235(O_{ϵ^1})	2.0
Mn(2)−Asp82(O_{δ^1})	2.13	2.08	2.1	Co(2)−Asp97(O_{δ^1})	2.2
Mn(2)−Asp82(O_{δ^2})	2.00	2.08	2.0	Co(2)−Asp97(O_{δ^2})	2.3
Mn(2)−Asp93(O_{δ^1})	2.05	2.05	2.1	Co(2)−Asp93(O_{δ^2})	2.1
Mn(2)− Glu280(O_{ϵ^2})	2.00	2.02	2.0	Co(2)− Glu235(O_{ϵ^2})	2.2
Mn(2)−Met(N)	2.09	2.07	2.1	Co(2)−Met(N)	2.2
Mn(1)−Met(O)	1.91	1.93	1.9	Co(1)−Met(O)	2.0
Mn(2)−Met(O)	2.71	2.82	2.8	Co(2)−Met(O)	2.2

[a] The distances for each molecule are reported separately (labeled *A* and *B*) as well as the average of the two (rounded to the tenths place to be more in line with the anticipated coordinate for a structure at the current resolution).

running parameters are specified in the figure captions for individual samples. The apo-*Ec*MetAP-I and *Pf*MetAP-II enzymes were incubated with substoichiometric amounts of Mn^{II} to suppress the isotropic signal from $[Mn(H_2O)_6]^{2+}$ and also to observe signals from the Mn^{II}-bound forms of MetAPs. Computer simulations were performed using XSophe (Bruker Biospin) (*23*).

Crystallization, Data Collection, and Refinement. [MnMn(*Pf*MetAP-II)]−L-Met was crystallized by sitting drop vapor diffusion at 21 °C (*12*). The crystals, of an average size of $0.3 \times 0.3 \times 0.4$ mm^3, were obtained within 30 days by mixing equal volumes (3 μL each) of 20 mg mL^{-1} of the [MnMn(*Pf*MetAP-II)] protein solution (containing 30 mM L-Met in 20 mM potassium acetate buffer at pH 4.5) and the reservoir solution containing 20% ethanol in 0.1 M Tris buffer at pH 8.5.

The [MnMn(*Pf*MetAP-II)]−L-Met crystals belong to space group $P6_4$ with unit cell parameters $a = b = 112.01$ Å and $c = 122.96$ Å. Prior to data collection, the crystals were equilibrated for 5 min in a mother liquor solution containing 30% glycerol as a cryoprotectant. The crystals were flash-cooled in liquid nitrogen on rayon loops, and data collection was performed under a continuous nitrogen stream at ∼100 K at the Stanford Synchrotron Radiation Laboratory (SSRL) beamline 9-1 ($\lambda = 1.5418$ Å). Reflections were integrated using MOSFLM (*24*) and scaled with SCALA of the CCP4 suite of programs (*25*) (Table 1). The 208 524 total reflections measured for [MnMn(*Pf*MetAP-II)]−L-Met were reduced to 38 795 unique reflections representing 99.7% of complete data to 2.3 Å resolution (Table 1).

The structure was determined by the molecular replacement method with AMORE (*26*, *27*) using the [CoCo(*Pf*MetAP-II)] structure (PDB entry 1XGM) (*12*) as a search model. The search was carried out with the data between 12.0 and 5.0 Å, and two molecules had a correlation coefficient of 70.2 ($R = 31.8\%$). Solvent flattening and 2-fold noncrystallographic averaging were employed to improve the quality of the electron-density map (*25*). The model was improved through iterative model building using the program O (*28*). During refinement, a bulk solvent correction allowed the inclusion of all low-resolution reflections and ∼5% of the data were randomly selected for cross validation (*29*). Model bias was removed for the incorporation of R_{free} calculation for cross validation by randomization using the simulated annealing routine of CNS (*29*) with an annealing temperature of 4000 K. Initial-position refinement of the rigid-body-refined model using 30.0−2.3 Å for the [MnMn(*Pf*MetAP-II)]−L-Met data followed by group *B*-factor refinement dropped the R_{free} to 31.9% and R_{cryst} to 28.7%. During the majority of refinement, noncrystallographic symmetry restraints were applied to restrict differences in symmetrically equivalent atoms. These restraints were released in the latter stages of refinement. The final model has been refined to the full-resolution range of data (Table 1) to a current R_{free} of 25.2% and R_{cryst} of 21.5%. The crystal structure of [MnMn(*Pf*MetAP-II)]−L-Met consists of all 590 possible protein residues, 4 Mn ions, and 325 water molecules per symmetry unit cell (Table 2). PROCHECK (*30*) analysis indicates that the model exhibits good geometry with a root-mean-square deviation from ideal bond lengths and angels of 0.011 Å and 2.20° and with all residues of the model lying in the allowed regions of the Ramachandran plot (Table 1).

RESULTS

Inhibition of [Mn(PfMetAP-II)] by L-Met. The specific activity of Mn^{II}-loaded *Pf*MetAP-II was determined at nine substrate concentrations (1−30 mM MGMM) in the presence of 0−200 mM L-Met. These data were plotted as activity versus substrate concentration and fit to a competitive inhibition equation using Sigma Plot software. L-Met was found to be a weak competitive inhibitor of Mn^{II}-loaded *Pf*MetAP-II with a K_i value of 150 ± 30 mM.

Electronic Absorption Spectroscopy. The electronic absorption spectrum of Co^{II}-loaded *Pf* MetAP-II reveals three

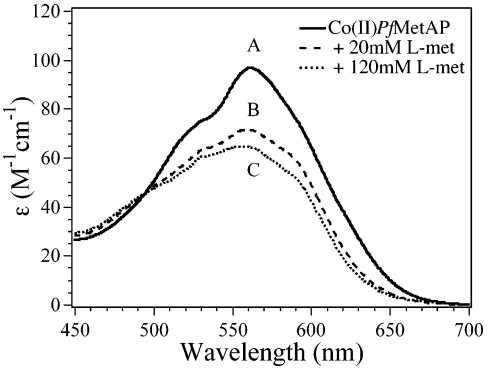

FIGURE 1: Electronic absorption spectrum of (A) [Co(*Pf*MetAP-II)], (B) [Co(*Pf*MetAP-II)] and 20 mM L-Met, and (C) [Co-(*Pf*MetAP-II)] and 120 mM L-Met. All electronic absorption spectra were recorded with 1 mM (*Pf*MetAP-II) with 2 equiv of Co^{II} added (25 mM HEPES at pH 7.5 and 150 mM KCl).

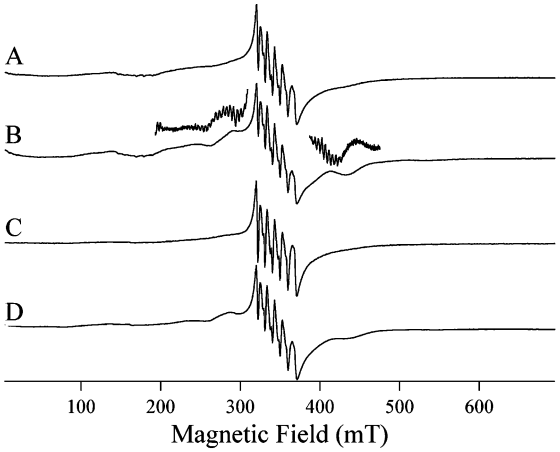

FIGURE 2: EPR spectra of [MnMn(*Ec*MetAP-I)] (A and B) and [MnMn(*Pf*MetAP-II)] (C and D). Spectra were recorded with 0.4 mT modulation amplitude with microwave powers and temperatures, respectively, of 1 mW and 10 K (A), 10 mW and 20 K (B), 0.1 mW and 10 K (C), and 10 mW and 20 K (D). The insets above trace B are second derivatives of B ($\partial^2\chi/\partial H^2$).

maxima with λ_{max} values of 525 nm ($\epsilon_{525} = 72\ M^{-1}\ cm^{-1}$), 562 nm ($\epsilon_{562} = 100\ M^{-1}\ cm^{-1}$), and 590 nm ($\epsilon_{590} = 93\ M^{-1}\ cm^{-1}$) (Figure 1A). These data are in good agreement with previously published results (*20*). Upon the addition of 20 mM L-Met to Co^{II}-loaded *Pf*MetAP-II, the intensity of the observed peaks decreased by approximately 25% (Figure 1B). The molar absorptivities further decreased after the addition of L-Met to a concentration of 120 mM, but the λ_{max} did not change (Figure 1C). The observed λ_{max} values and their corresponding molar absorptivities are consistent with the active-site Co^{II} ion in the L-Met complex residing in a distorted pentacoordinate environment.

EPR Spectra of [MnMn(PfMetAP-II)] and [MnMn(EcMetAP-I)]. The EPR spectra of [MnMn(*Pf*MetAP-II)] and [MnMn(*Ec*MetAP-I)], recorded at 10 K, are essentially indistinguishable (traces A and C of Figure 2) and are characteristic of mononuclear Mn^{II}, with $g_{eff} = 2.03$ and $A_{I=5/2}(^{55}Mn) = 9$ mT (*31*). Also evident in the spectra is a six-line pattern centered at $g = 4.15$ (166 mT) with $A_{av}(^{55}Mn) \sim 9.0$ mT. This signal is often attributed to $\Delta m_s = 2$ transitions that are formally forbidden for systems of high symmetry (*32*−*34*). Additional features were also observed at $g = 5.1$ (134 mT), $g = 2.4$ (290 mT), and $g = 1.6$ (434 mT); these features were weak and poorly resolved at 10 K

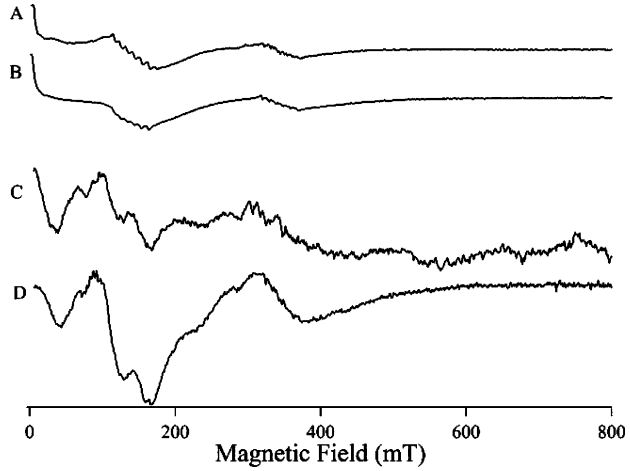

FIGURE 3: Comparison of high- and low-temperature parallel-mode spectra of [MnMn(*Pf*MetAP-II)] and [MnMn(*Ec*MetAP-I)]. Parallel-mode spectra of 1 mM [MnMn(*Pf*MetAP-II)] recorded at (A) 4.85 and (C) 40 K. Parallel-mode spectra of 1 mM [Mn(*Ec*MetAP-I)] recorded at (B) 5 and (D) 40 K. The applied EPR parameters were as follow: 9.39 GHz, spectrometer frequency; 20 mW, microwave power; 0.4 mT, modulation amplitude; and 2 mT s^{-1}, sweep rate.

(traces A and C of Figure 2) but increased in intensity at higher temperatures (traces B and D of Figure 2). Variable temperature studies (not shown) indicated a Boltzmann-like temperature dependence for these features, suggestive of excitation of higher energy doublets in a spin ladder, and second derivative EPR spectra (insets on trace B of Figure 2) identified the multiline structure of these features with a splitting of 0.45 mT.

Parallel-mode ($B_0||B_1$) EPR spectra of [MnMn(*Pf*MetAP-II)] and [MnMn(*Ec*MetAP-I)] (Figure 3) were recorded at various temperatures. At 5 K, the signals are dominated by an intense near-zero-field absorption at $g \geq 21$ (traces A and B of Figure 3). These signals are likely to originate from one or more inter-Kramers' doublet fine structure transitions for a mononuclear Mn^{II} center. Similar signals were observed for other Mn^{II} enzymes such as bacteriophage λ protein phosphatase and arginase (*35*−*38*). The $\Delta m_s = 2$ half-field transitions are also prominent, and there is some "bleed over" of the $g \sim 2$ six-line pattern. Thus, at 5 K, all of the spectral features in the parallel-mode signal can be attributed to mononuclear Mn^{II}. However, at higher temperatures (e.g., 40 K; traces C and D of Figure 3), additional features become apparent. There is a minimum feature at $g_{eff} = 4.2$ (165 mT), which is suggestive of an $S = 1$ spin system, a peak at $g_{eff} = 8.0$ (85 mT), which suggests an $S = 2$ spin system, a shoulder at $g_{eff} = 12$ (58 mT), and a broad feature extending out of the zero field that exhibits a minimum at $g_{eff} = 18$ that could arise from either or both an $S = 4$ or 5 spin system (*39*). These features displayed complex, Boltzmann-like temperature dependence, and although the signals could not be deconvoluted because of overlap in both the spectral and temperature domains, their resonance positions and temperature dependencies are consistent with them being due to non-Kramers' doublet transitions in an $S = 0, 1, ..., 5$ spin ladder (*40*, *41*). This, in turn, is completely consistent with two antiferromagnetically coupled Mn^{II} ions exhibiting modest exchange coupling ($J \ll 50\ cm^{-1}$). Strong support for this assignment comes from a clear hyperfine pattern on the $g = 8$ feature with a hyperfine splitting of 4.4 mT (*32*, *38*).

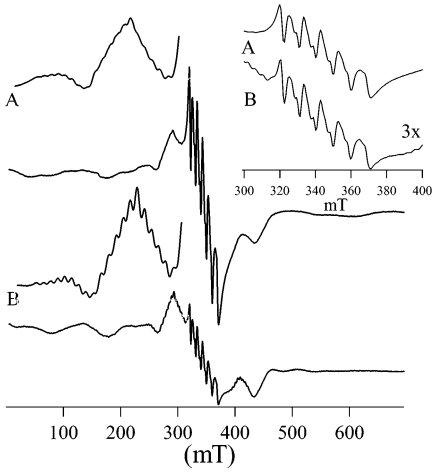

FIGURE 4: EPR spectrum of 1 mM [MnMn(*Ec*MetAP-I)]−L-Met (A) and [Mn(*Pf*MetAP-II)]−L-Met (B) complexes. These data were collected at 40 K using 20 mW, microwave power; 0.4 mT, modulation amplitude; and 2 mT s^{-1}, sweep rate. High-resolution scans of the region 220−320 mT at 40 K are shown as a "blow up" above each spectrum. Inset, comparison of the $g = 2$ region. The signal at $g = 2.03$ of [Mn(*Ec*MetAP-I)]−L-Met was multiplied by 3. The EPR parameters were 20 mW, microwave power; 1 mT, modulation amplitude; and 2 mT s^{-1}, scan rate.

EPR Spectra of [MnMn(EcMetAP-I)]−L-Met and [MnMn-(PfMetAP-II)]−L-Met. Parallel- and perpendicular-mode spectra were recorded for both [MnMn(*Ec*MetAP-I)] and [MnMn(*Pf*MetAP-II)] in the presence of the reaction product, L-Met. Figure 4 shows the perpendicular-mode spectra of [MnMn(*Ec*MetAP-I)]−L-Met and [MnMn(*Pf*MetAP-II)]−L-Met at 40 K. Clearly, both spectra contain the same spectral features as [MnMn(*Ec*MetAP-I)] and [MnMn(*Pf*MetAP-II)], although the intensities of the central six-line pattern, because of mononuclear Mn^{II}, is markedly decreased. In addition, the hyperfine patterns observed in the spectra of naked [MnMn(*Ec*MetAP-I)] and [MnMn(*Pf*MetAP-II)] (Figure 2B) are much better resolved in the L-Met-bound species and are clearly visible in the first derivative ($\partial\chi/\partial H$) traces (Figure 4). The observed hyperfine pattern at 290 mT and a less intense pattern at 408 mT consists of eleven lines with approximate relative intensities of 1:2:3:4:5:6:5:4:3:2:1 and a hyperfine coupling constant of ∼4.4 mT. This hyperfine pattern is diagnostic for exchanged coupled $Mn^{II}-Mn^{II}$ centers (*32*, *38*, *39*). The parallel-mode spectra of [MnMn-(*Ec*MetAP-I)]−L-Met and [MnMn(*Pf*MetAP-II)]−L-Met (Figure 5) are essentially indistinguishable from the spectra of the unbound forms of [MnMn(*Ec*MetAP-I)] and [MnMn-(*Pf*MetAP-II)], except that, as for the perpendicular-mode spectra, the hyperfine patterns are better resolved in the L-Met-bound species (Figure 6).

X-ray Crystal Structure of [MnMn(PfMetAP-II)] with L-Met. The X-ray crystal structure of [MnMn(*Pf*MetAP-II)] complexed with the reaction product L-Met was solved to 2.3 Å resolution. The comparison of the average *B* factor for the L-Met molecules (28.5 $Å^2$) and manganese ions (26.4 $Å^2$) in the two MnMn(PfMetAP-II) molecules is lower than that of the average *B* factor for all other non-hydrogen atoms (34.5 $Å^2$), indicating that the L-Met molecules and metal ions are present at high occupancy. The two manganese atoms are 3.4 Å apart compared to 3.3 Å in the [CoCo(*Pf*MetAP-II)] structure (Table 2 and Figure 7). The amino acid residues coordinated to the dinuclear Mn^{II} cluster are identical to those

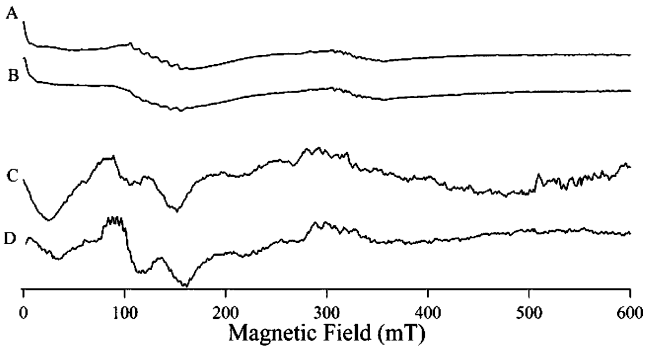

FIGURE 5: Parallel-mode spectra of 1 mM [MnMn(*Pf*MetAP-II)]−L-Met at (A) 4.85 and (C) 40 K and 1 mM [MnMn(*Ec*MetAP-I)]−L-Met at (B) 5 and (D) 40 K. The applied EPR parameters were as follow: 9.39 GHz, spectrometer frequency; 20 mW, microwave power; 0.4 mT, modulation amplitude; and 2 mT s^{-1}, sweep rate.

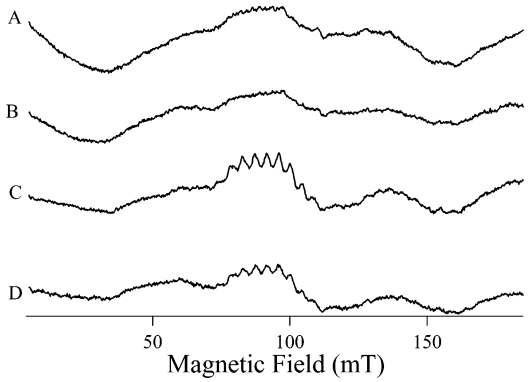

FIGURE 6: High resolution in parallel-mode EPR spectra of 1 mM [MnMn(*Pf*MetAP-II)]−L-Met recorded at (A) 40 and (B) 70 K and 1 mM [MnMn(*Ec*MetAP-I)]−L-Met recorded at (C) 40 and (D) 70 K. EPR-recording conditions were as follows: 9.39 GHz, spectrometer frequency; 20 mW, microwave power; 1 mT, modulation amplitude; and 2 mT s^{-1}, scan rate.

in the dinuclear Co^{II} structure with only minor perturbations in bond lengths and angles (Table 2 and Figure 7). Both Mn1 and Mn2 reside in a distorted trigonal bipyramidal geometry, and the lack of observable electron density between the two Mn^{II} ions suggests that the bridging water/hydroxide observed in the wild-type structure of [CoCo-(*Pf*MetAP-II)] has been replaced by L-Met. L-Met binds to the dinuclear Mn^{II} active site, where one of the carboxylate oxygen atoms binds to Mn1, while the N-terminal amine nitrogen atom binds to Mn2.

DISCUSSION

Recently, it was reported that both *Ec*MetAP-I and *Pf*MetAP-II contain a high- and low-affinity metal-binding site and that each enzyme is maximally active when only one metal-binding site is occupied (*18*−*20*, *42*). On the basis of the observed catalytic activity and the metal-binding constants for both sites, both *Ec*MetAP-I and *Pf*MetAP-II were proposed to function, *in vivo*, as a mononuclear enzyme. Additionally, the high-affinity metal-binding site was assigned as the histidine-containing site and, therefore, is the catalytically relevant metal-binding site (*19*, *21*). Recently, the human cytosolic AMPP, which has an identical active ligand to that of both *Ec*MetAP-I and *Pf*MetAP-II, was shown to be maximally stimulated by Mn^{II} ions (*43*). Moreover, this study also showed that only one Mn^{II} ion was required for full activity, providing the first evidence

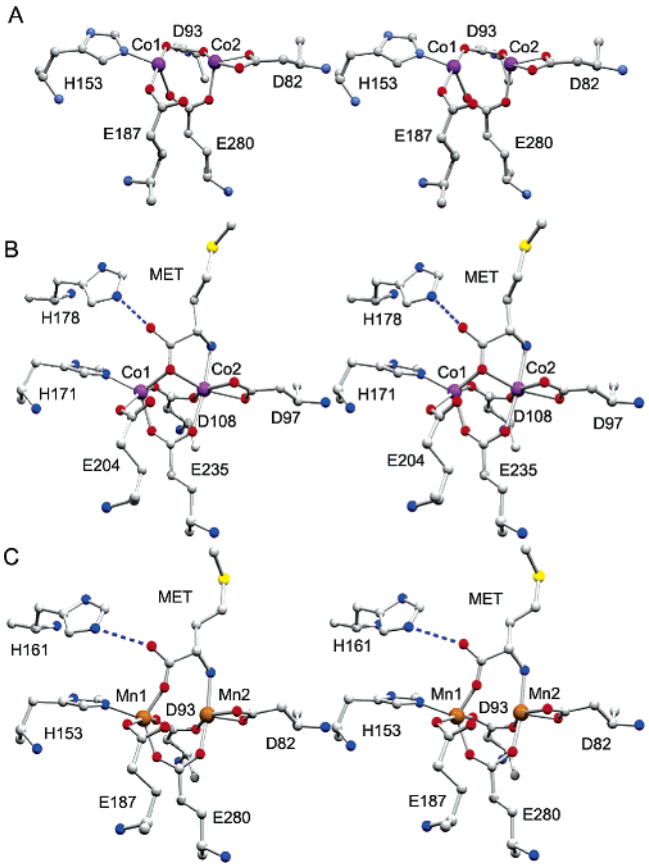

FIGURE 7: Active sites of (A) [CoCo(*Pf*MetAP-II)] (PDB entry 1XGM), (B) [CoCo(*Ec*MetAP-I)] complex with L-Met (PDB entry 1C21), and (C) [MnMn(*Pf*MetAP-II)]−L-Met. Color scheme for atoms are carbon, gray; oxygen, red; nitrogen, blue; sulfur, yellow; cobalt, magenta; and manganese, orange.

that AMPPs are also mononuclear enzymes, similar to MetAPs. To gain insight into the Mn^{II}-binding properties and the product-bound forms of both type-I and type-II MetAPs when Mn^{II} is the metal cofactor, we have recorded EPR spectra of the Mn^{II}-loaded forms of both enzymes.

The X-band EPR spectra of both [MnMn(*Ec*MetAP-I)] and [MnMn(*Pf*MetAP-II)] at 4 and 40 K exhibit a hyperfine split six-line signal centered at $g = 2$ and with $A_{I=5/2}(^{55}Mn) = 9$ mT, characteristic of mononuclear Mn^{II} and consistent with Mn^{II} ions being coordinated by oxygen- and nitrogen-containing ligands (*32*). In addition to the mononuclear Mn^{II} signal, the parallel- and perpendicular-mode EPR spectra of both the naked and L-Met-bound forms of [MnMn(*Ec*MetAP-I)] and [MnMn(*Pf*MetAP-II)] contain features that can only rationally be assigned to spin-coupled Mn^{II} ions and indicate that a polynuclear Mn^{II} center can be formed in the enzyme. X-ray crystallography shows that the enzyme can indeed form a dinuclear Mn^{II} center, and the EPR data are entirely consistent with a proportion of the sample being a dinuclear Mn^{II} system. Attempts were made to extract spin Hamiltonian parameters through computer simulations. Matrix diagonalization approaches have been successful for both mononuclear Mn^{II} (*44*) and dinuclear Mn^{II} (*39*). In the present case, both the spectral and temperature-dependence resolution were insufficient to fully deconvolute spectral features. Thus, an accurate value for the exchange coupling could not be obtained, and this parameter remained a variable in the simulations. The lack of single-crystal data also dictated that the geometric relationships between the *g* tensors of the Mn^{II} ions and the inter-Mn^{II} vector were unknown. An additional complication arises from the contribution of interdoublet forbidden transitions, which are nonnegligible at the X band and require that simulations take into account all of the $S = 0, 1, 2, ..., 5$ spin states simultaneously. The time required for each simulation of the dinuclear component of the spectra of [MnMn(*Ec*MetAP-I)] and [MnMn(*Pf*MetAP-II)] is, therefore, measured in days (weeks, if the hyperfine interaction is included) rather than minutes or hours. Because of the large numbers of variables, exact line-shape simulations were not obtained but systematic variation of certain parameters was carried out based on temperature dependence, crystallographic data, and earlier studies. The simulations indicate an inter-Mn^{II} distance of $3.54 > r > 3.14$ Å and thus provide support for the proposal that the EPR signal is indeed due to the crystallographically identified dinuclear Mn^{II} center.

One of the steps within the proposed catalytic mechanism of MetAPs that has been largely overlooked is the structure of the product-bound form of the enzyme. Initially, the electronic absorption spectrum of [CoCo(*Pf*MetAP-II)] was recorded both in the absence and presence of 120 mM L-Met. No change in the λ_{max} values was observed; however, the molar absorptivities decreased, suggesting that L-Met does bind to the active-site Co^{II} ions. The molar absorptivities of the [CoCo(*Pf*MetAP-II)]−L-Met complex are consistent with Co^{II} coordination numbers of five. The fact that the Co^{II} coordination number remains the same upon L-Met binding suggests that L-Met displaces a labile Co^{II} ligand, most likely a water/hydroxide. Conversely, the previously reported electronic absorption spectrum of the [CoCo(*Ec*MetAP-I)]−L-Met complex indicated that the Co^{II} coordination geometry changed from trigonal bipyramidal to distorted octahedral (*13*, *45*). These data suggest that, unlike the Co^{II} centers in *Pf*MetAP-II, the Co^{II} centers in *Ec*MetAP-I expanded their coordination number.

The fact that the electronic absorption data suggest that L-Met binds differently to type-I MetAPs than type-II MetAPs indicates that the two types of MetAPs may have some mechanistic differences. To further examine the product-bound form of both type-I and type-II MetAPs, EPR spectra of [MnMn(*Ec*MetAP-I)] and [MnMn(*Pf*MetAP-II)] in the presence of L-Met were recorded. Upon the addition of L-Met to [MnMn(*Ec*MetAP-I)], the signals observed at $g = 2.4$ and 1.7 become more intense than in the resting enzyme and exhibit a well-resolved eleven-line hyperfine splitting with $A = 4.4$ mT. These data are indicative of the formation of a dinuclear Mn^{II}−Mn^{II} center that is magnetically coupled (Figure 4) (*32*, *38*). These data suggest that the two Mn^{II} centers are in close proximity within the MetAP active site, which allows magnetic coupling, or that there is a third bridging moiety that facilitates such coupling. Interestingly, L-Met appears to increase either the resolution or the relative amplitude of the multiline EPR signal because of dinuclear Mn, although it is unclear whether this is due to an L-Met-mediated decrease in the lability of one or more of the Mn ions or whether L-Met binding renders the multiline signal more easily observable because of the reduction of strains in the zero-field splitting parameters. Further, the higher resolution of the hyperfine lines in the L-Met-bound forms may be indicative of a reduction in the strain terms (either in *g* or in zero-field splitting parameters). The spectrum of [MnMn(*Pf*MetAP-II)]−L-Met also exhibits

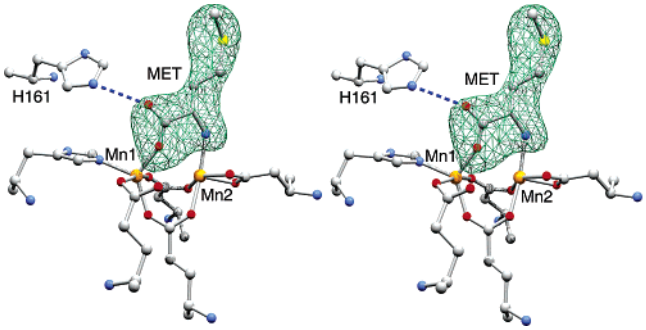

FIGURE 8: Omit $F_o - F_c$ electron-density map calculated to 2.3 Å resolution for the [MnMn(*Pf*MetAP-II)]−L-Met complex (Table 1). Color scheme is same as in Figure 7.

signals at $g = 2.4$ and 1.7, but the hyperfine pattern is not well-resolved and is less pronounced, indicating that most of the Mn^{II} ions in the sample are uncoupled. Parallel-mode spectra of the [MnMn(*Ec*MetAP-I)]−L-Met and [MnMn(*Pf*MetAP-II)]−L-Met complexes were also recorded (Figure 5 and 6). The parallel-mode spectrum of [MnMn(*Ec*MetAP-I)]−L-Met exhibits a multiline signal at $g = 7.6$ with a hyperfine coupling constant of 4.4 mT, indicative of a dinuclear Mn^{II}−Mn^{II} that is antiferromagnetically coupled. This multiline pattern was not detected in the parallel-mode EPR spectrum of [MnMn(*Pf*MetAP-II)]−L-Met. These data are consistent with the suggestion that the dinuclear Mn^{II} center in *Pf*MetAP-II is not as magnetically coupled.

The observed EPR spectra of [MnMn(*Ec*MetAP-I)]−L-Met and [MnMn(*Pf*MetAP-II)]−L-Met contain signals with similar *g* values, and these signals exhibit similar temperature dependencies. These data suggest that the observed EPR signals originate from the same type of transition for both enzymes. The major difference arises from the relative intensities of the respective signals assigned to the mono- and dinuclear Mn^{II} species in [Mn(*Pf*MetAP-II)]−L-Met and [MnMn(*Ec*MetAP-I)]−L-Met (Figure 4). For example, the perpendicular-mode six-line signal at $g = 2.03$ ($A = 8.8$ mT) is 3-fold more intense in [MnMn(*Pf*MetAP-II)]−L-Met and has been shown to be due to mononuclear Mn^{II} ions residing in octahedral or trigonal bipyramidal environments with oxygen or nitrogen ligands (*32*). Similarly, in the parallel mode, the six-line hyperfine pattern observed at $g = 4.2$ with $A = 8.8$ is much better resolved and more pronounced in [MnMn(*Pf*MetAP-II)]−L-Met than in [MnMn(*Ec*MetAP-I)]−L-Met. These data also suggest that the dinuclear Mn^{II} sites in type-I and type-II MetAPs in the presence of L-Met reside in different environments, which results in an increased amount of mononuclear Mn^{II} sites in the [MnMn(*Pf*MetAP-II)]−L-Met complex.

To further characterize the binding of L-Met to [MnMn(*Pf*MetAP-II)], the enzyme was crystallized in the presence of L-Met and the X-ray crystal structure was determined to 2.3 Å resolution (Figures 7 and 8). Like all of the structures reported for MetAP−inhibitor complexes, the methionine

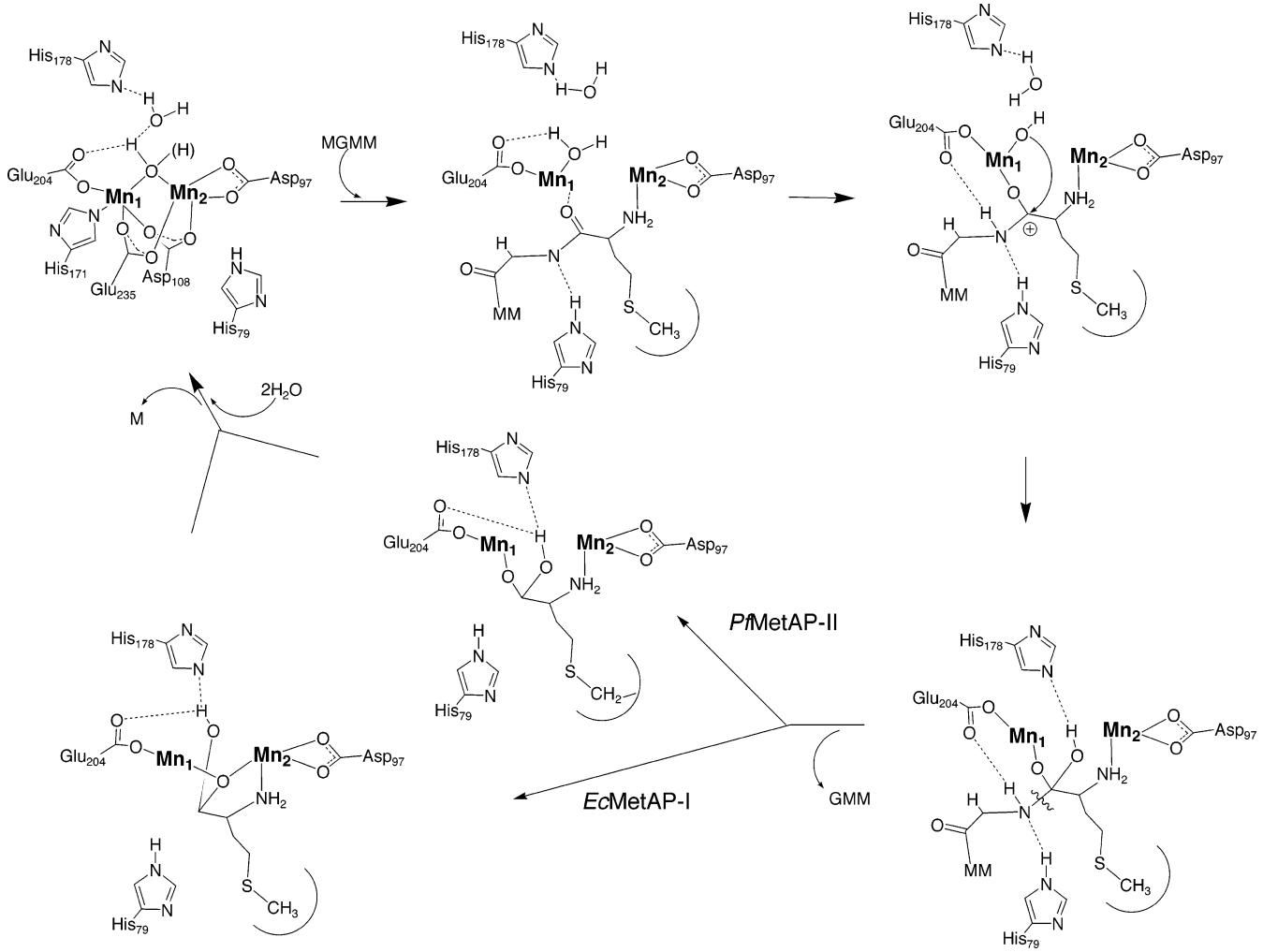

FIGURE 9: Proposed catalytic mechanism for a dinuclear Mn^{II}MetAP enzyme.

group of L-Met resides in a well-defined hydrophobic pocket adjacent to the dinuclear Mn^{II} active site (*13*, *45*). L-Met binding to [MnMn(*Pf*MetAP-II)] results in a species in which the Mn−Mn distance is 3.4 Å; the Co−Co distance in uncomplexed [CoCo(*Ec*MetAP-I)] is 3.3 Å. In both species, the coordination number remains five, consistent with the electronic absorption data for [CoCo(*Ec*MetAP-I)]. No active-site ligands are displaced upon L-Met binding except the water molecule, which bridges the two Co^{II} ions in the wild-type structure. This bridging water molecule is displaced by one of the carboxylate oxygen atoms of L-Met. However, this carboxylate oxygen atom does not bridge between the two Mn^{II} ions but is terminal on M1, consistent with the EPR data obtained on the [MnMn(*Pf*MetAP-II)]−L-Met complex. The N-terminal amine nitrogen of L-Met (N1) resides 2.1 Å from Mn2, indicating that it is bound to Mn2. In both enzymes, the active-site histidine [His161 of *Pf*MetAP-II (3.1 Å) and His178 of *Ec*MetAP-I (2.6 Å)] forms a hydrogen bond with the second oxygen of the carboxylate group of L-Met.

The observed binding mode of L-Met to [MnMn(*Pf*MetAP-II)] is different from that reported for the binding of L-Met to the active site of [CoCo(*Ec*MetAP-I)] (Figure 7) (*45*). In the [CoCo(*Ec*MetAP-I)]−L-Met structure, the carboxylate oxygen atom of L-Met bridges between the two Co^{II} centers, while the N-terminal amine nitrogen atom binds to Co2. The observed differences in the X-ray crystal structures of [CoCo(*Ec*MetAP-I)]−L-Met and [MnMn(*Pf*MetAP-II)]−L-Met likely account for the differences in magnetic coupling observed between [MnMn(*Ec*MetAP-I)]−L-Met and [MnMn(*Pf*MetAP-II)]−L-Met. A bridging carboxylate oxygen, as observed in the [CoCo(*Ec*MetAP-I)]−L-Met structure, will provide a stronger magnetic coupling interaction for the two Mn^{II} ions, with [MnMn(*Ec*MetAP-I)]−L-Met accounting for the increased coupling between the two Mn^{II} ions in [MnMn(*Ec*MetAP-I)]−L-Met. The lack of a single atom bridge in the [MnMn(*Pf*MetAP-II)]−L-Met structure indicates that theses two MetAP enzymes bind the product differently.

On the basis of the data presented herein as well as all of the kinetic, spectroscopic, and X-ray crystallographic data reported to date on MetAPs, a refined mechanism of action for *Ec*MetAP-I and *Pf*MetAP-II is proposed (Figure 9) (*45*). On the basis of the recently proposed mechanism for the leucine aminopeptidase from *Aeromonas proteolytica* (*46*, *47*), the first step in catalysis for MetAPs is likely recognition of the N-terminal methionine side chain by the hydrophobic pocket adjacent to the metalloactive site (*13*, *45*). Next, the peptide carbonyl oxygen coordinates to the histidine-ligated divalent metal ion. Hydrogen-bond formation between His79 and the backbone N−H scissile peptide bond has been proposed based on X-ray crystallographic results, thereby stabilizing the leaving group (*13*, *45*). In addition, Glu204, which is also a ligand to the histidine-containing divalent metal ion, was proposed to be a proton acceptor/donor in the catalytic process (*13*, *45*). Because the N-terminal amine nitrogen of the substrate forms a hydrogen bond with D97 based on X-ray crystallography (*13*, *45*), in the absence of a second metal ion, D97 likely assists to position the substrate properly in the active site for formation of the transition-state intermediate (*48*). In the presence of a dinuclear site, the second metal ion coordinates the N-terminal amine (*13*, *45*). Next, the product-forming C−N bond-breaking step occurs followed by the release of the cleaved peptide. On the basis of the date presented herein, the structure of the product-bound form of *Pf*MetAP-II contains a single carboxylate oxygen atom bound to M1 with the N-terminal amine bound to M2. Moreover, this L-Met-binding mode is different from that observed for L-Met binding [CoCo(*Ec*MetAP-I)] (*13*, *45*). Therefore, the catalytic mechanisms of type-I MetAPs may differ somewhat from type-II enzymes; however, in the absence of a second metal ion, the proposed mechanisms for type-I and type-II MetAPs would remain identical (*48*). The fact that the product, methionine, would be weakly bound to Mn-loaded *Pf*MetAP-II under physiological conditions is evidenced by its weak K_i (150 mM). Finally, the active site adds two water molecules: one that binds to the divalent metal ion and one that bridges between the coordinated water molecule and H178.

REFERENCES

1. Bradshaw, R. A., Brickey, W. W., and Walker, K. W. (1998) N-Terminal Processing: The Methionine Aminopeptidase and N^{α}-Acetyl Transferase Families, *Trends Biochem. Sci. 23*, 263.
2. Bradshaw, R. A. (1989) Protein Translocation and Turnover in Eukaryotic Cells, *Trends Biochem. Sci. 14*, 276.
3. Arfin, S. M., and Bradshaw, R. A. (1988) Cotranslational Processing and Protein Turnover in Eukaryotic Cells, *Biochemistry 27*, 7979.
4. Hirel, P.-H., Schmitter, J.-M., Dessen, P., Fayat, G., and Blanquet, S. (1989) Extent of N-Terminal Methionine Excision from *Escherichia coli* Proteins Is Goverened by the Side-Chain Length of the Penultimate Amino Acid, *Proc. Natl. Acad. Sci. U.S.A. 86*, 8247.
5. Meinnel, T., Mechulam, Y., and Blanquet, S. (1993) Methionine as Translation Start Signal−A Review of the Enzymes of the Pathway in *Escherichia coli*, *Biochimie 75*, 1061.
6. Chang, S.-Y. P., McGary, E. C., and Chang, S. (1989) Methionine Aminopeptidase Gene of *Escherichia coli* Is Essential for Cell Growth, *J. Bacteriol 171*, 4071.
7. Li, X., and Chang, Y.-H. (1995) Amino-Terminal Protein Processing in *Saccharomyces cerevisiae* Is an Essential Function That Requires Two Distinct Methionine Aminopeptidases, *Proc. Natl. Acad. Sci. U.S.A. 92*, 12357.
8. Miller, C. G., Kukral, A. M., Miller, J. L., and Movva, N. R. (1989) *Pepm* Is an Essential Gene in *Salmonella typhimurium*, *J. Bacteriol. 171*, 5215.
9. Griffith, E. C., Su, Z., Turk, B. E., Chen, S., Chang, Y.-H., Wu, Z., Biemann, K., and Liu, J. O. (1997) Methionine Aminopeptidase (Type 2) Is the Common Target for Angiogenesis Inhibitors Agm-1470 and Ovalicin, *Chem. Biol. 4*, 461.
10. Sin, N., Meng, L., Wang, M. Q., Wen, J. J., Bornmann, W. G., and Crews, C. M. (1997) The Anti-Angiogenic Agent Fumagillin Covalently Binds and Inhibits the Mathionine Aminopeptidase, Metap-2, *Proc. Natl. Acad. Sci. U.S.A. 94*, 6099.
11. Arfin, S. M., Kendall, R. L., Hall, L., Weaver, L. H., Stewart, A. E., Matthews, B. W., and Bradshaw, R. A. (1995) Eukaryotic Methionyl Aminopeptidases: Two Classes of Cobalt-Dependent Enzymes, *Proc. Natl. Acad. Sci. U.S.A. 92*, 7714.
12. Tahirov, T. H., Oki, H., Tsukihara, T., Ogasahara, K., Yutani, K., Ogata, K., Izu, Y., Tsunasawa, S., and Kato, I. (1998) Crystal Structure of the Methionine Aminopeptidase from the Hyperthermophile, *Pyrococcus Furiosus*, *J. Mol. Biol. 284*, 101.
13. Lowther, W. T., Orville, A. M., Madden, D. T., Lim, S., Rich, D. H., and Matthews, B. W. (1999) *Escherichia coli* Methionine Aminopeptidase: Implications of Crystallographic Analyses of the Native, Mutant, and Inhibited Enzymes for the Mechanism of Catalysis, *Biochemistry 38*, 7678.
14. Roderick, L. S., and Matthews, B. W. (1993) Structure of the Cobalt-Dependent Methionine Aminopeptidase from *Escherichia coli*: A New Type of Proteolytic Enzyme, *Biochemistry 32*, 3907.
15. Liu, S., Widom, J., Kemp, C. W., Crews, C. M., and Clardy, J. (1998) Structure of the Human Methionine Aminopeptidase-2 Complexed with Fumagillin, *Science 282*, 1324.
16. Oefner, C., Douangamath, A., D'Arcy, A., Hafeli, S., Mareque, D., MacSweeney, A., Padilla, J., Pierau, S., Schulz, H., Thormann,

M., Wadman, S., and Dale, G. E. (2003) The 1.15 Å Crystal Structure of the *Staphylococcus aureus* Methionyl-Aminopeptidase and Complexes with Triazole-Based Inhibitors, *J. Mol. Biol. 332*, 13.
17. Walker, K. W., and Bradshaw, R. A. (1998) Yeast Methionine Aminopeptidase I Can Utilize Either Zn^{II} or Co^{II} as a Cofactor: A Case of Mistaken Identity, *Protein Sci. 7*, 2684.
18. D'souza, V. M., and Holz, R. C. (1999) The Methionyl Aminopeptidase from *Escherichia coli* Is an Iron(II) Containing Enzyme, *Biochemistry 38*, 11079.
19. D'souza, V. M., Bennett, B., Copik, A. J., and Holz, R. C. (2000) Characterization of the Divalent Metal Binding Properties of the Methionyl Aminopeptidase from *Escherichia coli*, *Biochemistry 39*, 3817.
20. Meng, L., Ruebush, S., D'souza, V. M., Copik, A. J., Tsunasawa, S., and Holz, R. C. (2002) Overexpression and Divalent Metal Binding Studies for the Methionyl Aminopeptidase from *Pyrococcus furiosus*, *Biochemistry 41*, 7199.
21. Cosper, N. J., D'souza, V., Scott, R., and Holz, R. C. (2001) Structural Evidence That the Methionyl Aminopeptidase from *Escherichia coli* Is a Mononuclear Metalloprotease, *Biochemistry 40*, 13302.
22. Wang, J., Sheppard, G. S., Lou, P., Kawai, M., Park, C., Egan, D. A., Schneider, A., Bouska, J., Lesniewski, R., and Henkin, J. (2003) Physiologically Relevant Metal Cofactor for Methionine Aminopeptidase-2 Is Manganese, *Biochemistry 42*, 5035.
23. Griffin, M., Muys, A., Noble, C., Wang, D., Eldershaw, C., Gates, K. E., Burrage, K., and Hanson, G. R. (1999) Xsophe, a Computer Simulation Software Suite for the Analysis of Electron Paramagnetic Spectrs, *Mol. Phys. Rep. 26*, 60.
24. Powell, H. R. (1999) The Rossmann Fourier Autoindexing Algorithm in Mosflm, *Acta Crystallogr., Sect. D 55*, 1690.
25. Collaborative Computational Project, No. 4 (1994) *Acta Crystallogr., Sect. D 50*, 760−763.
26. Navaza, J. (2001) Implementation of Molecular Replacement in Amore, *Acta Crystallogr., Sect. D 57*, 1367.
27. Oldfield, T. J. (2001) X-Ligand: An Application for the Automated Addition of Flexible Ligands into Electron Density, *Acta Crystallogr., Sect. D 57*, 696.
28. Jones, T. A., Zou, J.-Y., Cowan, S. W., and Kjeldgaard, M. (1991) Improved Methods for the Building of Protein Models in Electron Density Maps and the Location of Errors in These Models, *Acta Crystallogr., Sect. A 47*, 110.
29. Brunger, A. T., Adams, P. D., Clore, G. M., DeLano, W. L., Gros, P., Grosse-Kunstleve, J. S., Jiang, J., Kuszewski, J., Nilges, M., Pannu, N. S., Read, R. J., Rice, L. M., Simonson, T., and Warren, G. L. (1998) Crystallography and NMR system: A new software suite for macromolecular structure determination, *Acta Crystallogr., Sect. D 54*, 905−921.
30. Laskowski, R. A., Moss, D. S., and Thornton, J. M. (1993) Main-Chain Bond Lengths and Bond Angles in Protein Structures, *J. Mol. Biol. 231*, 1049.
31. D'souza, V. M., Brown, R. S., Bennett, B., and Holz, R. C. (2004) Charaterization of the Active Site and Insight into the Binding Mode of the Anti-Angiogenesis Agent Fumagillin to the Mn^{II}-Loaded Methionyl Aminopeptidase from *Escherichia coli*, *J. Eur. Biochem.*, manuscript submitted.
32. Reed, G. H., and Markham, G. D. (1984) *Biol. Magn. Reson. 6*, 73.
33. Griscom, D. L., and Griscom, R. E. (1967) *J. Chem. Phys. 47*, 2711.
34. Schreurs, J. W. H. (1978) *J. Chem. Phys. 69*, 2151.
35. Whiting, A. K., Boldt, Y. R., Hendrich, M. P., Wackett, L. P., and Que, L. (1996) Manganese(II)-Dependent Extradiol-Cleaving Chatechol Dioxygenase from *Arthrobacter globiformis* Cm-2, *Biochemistry 35*, 160.
36. Reiter, T. A., Reiter, N. J., and Rusnak, F. (2002) Mn^{2+} Is a Native Metal Ion Activator for Bacteriophage λ Protein Phosphatase, *Biochemistry 41*, 15404.
37. Rusnak, F., Yu, L., Todorovic, S., and Mertz, P. (1999) Interaction of Bacteriophage Λ Protein Phosphatase with Mn^{II}: Evidence for the Formation of a $[Mn^{II}]_2$ Cluster, *Biochemistry 38*, 6943.
38. Reczkowski, R. S., and Ash, D. E. (1992) EPR Evidence for Binuclear Mn^{II} Centers in Rat Liver Arginase, *J. Am. Chem. Soc. 114*, 10992.
39. Golombek, A. P., and Hendrich, M. P. (2003) Quantitative Analysis of Dinuclear Manganese(II) EPR Spectra, *J. Magn. Reson. 165*, 33.
40. Khangulov, S. V., Pessiki, P. J., Barynin, V. V., Ash, D. E., and Dismukes, G. C. (1995) Determination of the Metal Ion Separation and Energies of the Three Lowest Electronic States of Dimanganese(II, II) Complexes and Enzymes: Catalase and Liver Arginase, *Biochemistry 34*, 2015.
41. Khangulov, S. V., Sossong, T. M. J., Ash, D. E., and Dismukes, G. C. (1998) L-Arginine Binding to Liver Arginase Requires Proton Transfer to Gateway Residue His141 and Coordination of the Guanidinium Group to the Dimanganese(II, II) Center, *Biochemistry 37*, 8539.
42. D'souza, V. M., Swierczek, S. I., Cosper, N. J., Meng, L., Ruebush, S., Copik, A. J., Scott, R. A., and Holz, R. C. (2002) Kinetic and Structural Characterization of Manganese(II)-Loaded Methionyl Aminopeptidases, *Biochemistry 41*, 13096.
43. Cottrell, G., Hooper, N. M., and Turner, A. J. (2000) Cloning, Expression, and Characterization of the Human Cytosolic Aminopeptidase: A Single Manganese(II)-Dependent Enzyme, *Biochemistry 39*, 15121.
44. Coffino, A. R., and Peisach, J. "Simulation of Mn^{II} EPR Spectra Using a Full Spin-Hamiltonian Approach." (1996) *J. Magn. Reson. B. 111*, 127.
45. Lowther, T. W., Zhang, Y., Sampson, P. B., Honek, J. F., and Matthews, B. W. (1999) Insights into the Mechanism of *E. coli* Methionine Aminopeptidase from the Structural Analysis of Reaction Products and Phosphorous-Based Transition State Analogs, *Biochemistry 38*, 14810.
46. Ustynyuk, L., Bennett, B., Edwards, T., and Holz, R. C. (1999) Inhibition of the Aminopeptidase from *Aeromonas proteolytica* by Aliphatic Alchalols. Characterization of the Hydrophobic Substrate Recognition Site, *Biochemistry 38*, 11433.
47. Stamper, C., Bienvenue, D., Moulin, A., Bennett, B., Ringe, D., Petsko, G., and Holz, R. C. (2004) Spectroscopic and X-ray Crystallographic Characterization of the Bestatin-Bound Form of the Aminopeptidase from *Aeromonas proteolytica*, *Biochemistry 43*, 9620.
48. Copik, A. J., Swierczek, S. I., Lowther, W. T., D'souza, V., Matthews, B. W., and Holz, R. C. (2003) Kinetic and Spectroscopic Characterization of the H178a Mutant of the Methionyl Aminopeptidase from *Escherichia coli*, *Biochemistry 42*, 6283.

BI048123+